Mass Use In 2 µm Laser Driven Tin Plasma Using Sheet Targets

Y. Mostafa,[1, 2] L. Behnke,[1, 2] D. J. Engels,[1, 2] and O. O. Versolato[1, 2]
[1)] *Advanced Research Center for Nanolithography, Science Park 106, 1098 XG Amsterdam, The Netherlands*
[2)] *Department of Physics and Astronomy, and LaserLaB, Vrije Universiteit Amsterdam, De Boelelaan 1081, 1081 HV Amsterdam, The Netherlands*

(*Electronic mail: o.versolato@arcnl.nl)

(Dated: 22 September 2025)

We investigate the mass use of 2 µm wavelength laser driven tin plasmas as formed from thin tin sheet targets, and identify a key dependence of the efficiency (CE), of converting laser light into useful EUV photons, on the tin volume overlapping the laser beam. For plasmas driven under a CE-optimized laser intensity, 85 µm beam diameter and 11 ns pulse duration, an optimum overlap volume is approximately 2×10^{-15} m^3, a number relevant for nanolithography applications. Generating plasma using thicker tin sheets results in excess mass with no increase in CE while using thinner sheets leads to laser burnthrough behavior, and decreasing CE. We further show the effect of laser burning through targets of insufficient mass on EUV emission anisotropy and emission surface morphology through observations of time-dependent EUV emission, side-view EUV images, and transmitted laser light.

I. INTRODUCTION

Recent work[1] demonstrated the efficient generation of extreme ultraviolet (EUV) light from laser-produced plasma (LPP) driven by 2 µm wavelength laser light as an alternative for 10 µm CO_2 gas LPP currently employed in EUV lithography machines for high-volume-manufacturing of semiconductor devices. This makes 2 µm LPP a particularly promising candidate to power future EUV nanolithography, also given the promise of high-efficiency, high-power solid-state laser technology near 2 µm[2–4]. Besides high conversion efficiency (CE, $\sim 4\%$ compared to the industry's 5-6%[5,6]) of converting 2 µm drive laser power to useful, in-band ($13.5 \pm 1\%$ nm) EUV photons[7,8], also the required amount of tin needed to sustain the CE of is particular interest. High mass use efficiency is desirable in a LPP source of EUV. Excess supplied mass supplied by tin droplets or preformed sheets may contribute to excess neutral of ionized "debris" (i.e. unwanted remnant particulates), that may negatively affect nearby sensitive optics. In case of *mass-limited* plasma sources[9,10], only the minimum mass required to sustain the plasma is supplied to minimize debris[11].

Previous studies have demonstrated the effect of droplet size on the efficiency of 1- and 2-µm laser-driven plasma EUV sources[7,12]. In such studies, the dependency of the CE on droplet size is shown for non-preformed target experiments and on the sheet diameter for preformed targets. However, no investigation of the dependence of CE on target thickness, or, rather, the amount of mass overlapping the laser beam was yet performed for such LPPs. Furthermore, previous studies did not extend to the range of droplet sizes in which mass-limited behavior would be observed. In order to understand the mass use rate (i.e., the mass use per nanosecond exposure by the main-pulse) and to obtain a mass-optimized plasma, we aim to investigate the full range of mass available to interact with the laser beam. Other studies[13] have investigated the mass use rate and its dependence on laser wavelength and intensity for solid tin targets for laser wavelengths other than 2 µm. We aim to examine the mass use of plasma formed from preformed liquid tin targets under conditions relevant for EUV nanolithography albeit at a laboratory-scale 10 Hz repetition rate that lies well below the industry's several 10 kHz.

In this work, we demonstrate the mass use efficiency of 2-µm-wavelength laser-produced plasma and highlight its dependence on target thickness overlapping the laser beam. We show mass-limited laser-produced plasmas which exhibit low energy efficiency due to mass deficit. The key parameter is found to be the liquid volume overlapping the laser beam, a clear predictor of mass-use efficiency.

II. EXPERIMENT

We employ an experimental setup similar to that of Ref. 1 and briefly summarize the key workings in the following. In a vacuum chamber maintained at $\sim 10^{-6}$ mbar, we stream droplets of liquid tin through a nozzle. The tin droplets can be varied in diameter by controlling the volumetric flow rate in tandem with applying a suitable modulation to the nozzle. The resulting liquid stream is broken into droplets of consistent diameter.

In the experiments, first a low-energy 1 µm wavelength pre-pulse laser is fired onto a tin droplet inducing hydrodynamic deformation[14,15] to produce thin tin sheet targets. We use different pre-pulse laser energies E_p fired onto different diameters of tin droplets D_0, and change the pre-pulse to main-pulse delay time. This variation in D_0, E_p and delay results in tin sheets with various thicknesses and diameters[14,15] as shown in Fig. 1(a,b). After the predetermined delay, a spatially and temporally flat-top 2 µm laser beam with an energy enclosed within the FWHM of the spatial profile E_encl of 75% (cf. Ref. 1 where the E_encl concept was introduced as a metric of beam quality) is fired onto the tin sheet generating the plasma. The liquid tin target preparation is illustrated in Fig. 1. An example of the droplet deformation into a thin sheet is shown in Fig. 1(a). After the pre-pulse laser impact, the droplet expands radially and is propelled in the direction of the beam. At the hydrodynamic apex time t_apex, the sheet retracts due to

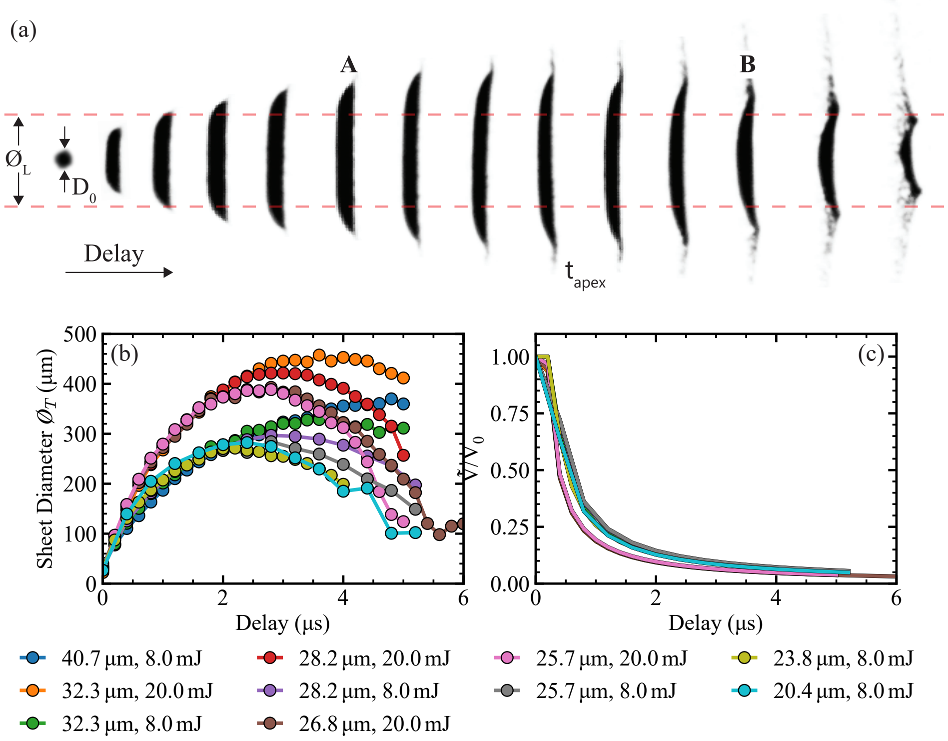

FIG. 1. Tin droplet deformation and expansion. (a) Side-view shadowgraphy images of the preshaping of a 20 µm diameter tin droplet. Pre-pulse laser impacts from the left propelling and shaping the droplet with initial diameter D_0. A main-pulse laser diameter $Ø_L$ is indicated with the dashed line. The sheet reaches maximum diameter at the hydrodynamic apex time t_{apex} after which it contracts. Sheets **A** and **B** have similar sheet diameters but different average thicknesses. (b) The sheet diameter $Ø_T$ as a function of the expansion time (pre-pulse to main-pulse delay) for different droplet sizes and pre-pulse energies. (c) The calculated tin mass overlapping the main-pulse (see the main text) as a function of time.

the surface tension of the liquid[14–16]. Late-time sheets may have the same diameter as early-time sheets, but will be thinner due to the continuous mass loss during the expansion, and retraction processes[17]. In Fig. 1(b), the expansion and retraction trajectories of all initial droplet size and pre-pulse energy combinations used in this study are shown as a function of time after pre-pulse impact.

The choice of a main-pulse with a flat spatial profile is motivated as follows. First, a uniform intensity illumination of the tin sheet results in uniform laser ablation characteristics relevant for the current study of mass use. Second, we aim to generate and study higher-CE plasmas driven by 2 µm laser light, relevant for EUV nanolithography; the highest CE values are obtained with flat-top profiles cf. Ref. 1.

The generated tin plasma is studied using four calibrated EUV photodiodes placed at varying angles with respect to the direction opposite to the laser light propagation , more specifically at 30°, 41°, 64° and 114° (given the cylindrical symmetry, a single angle fully describes the relative positions; emission towards a 180° angle indicates emission along the laser light propagation direction). We additionally place two fast EUV photodiodes, which enable a time-resolved observation of the emission, at angles 21° (forward, i.e. towards the location of a hypothetical light collection optic that would be situated towards the laser's origin) and 159° (backward) with respect to the direction opposite to the laser light propagation. As per our convention, the laser propagation direction is considered as the "backward direction", which corresponds to an angle of 180°. The EUV-emitting surface is captured using the EUV imaging system placed at 90° with respect to the direction opposite to the laser light propagation. The main-pulse laser energy is measured before the pulse is directed into the vacuum chamber and is corrected for transmission through the vacuum window. We measure the transmission of the vacuum window before and after the experimental studies and interpolate the transmission drop using an exponential function. This interpolation assumes a constant tin deposition rate per laser shot onto the window. Based on intermediate measurements of intensity dependence of the CE, we re-calibrate the required input energy to account for the decreased transmission. The temporal profile of the laser pulse is measured before the vacuum chamber using fast photodiodes paired with a 2 µm wavelength band-pass filter. At the vacuum chamber exit, we additionally measure the escaped laser light in a similar manner, using a wavelength-selecting filter and a fast photodiode aimed at a beam dump. Due to the high NA of the laser imaging system on the input side, some laser light is clipped at the exit by the vacuum windows. Accordingly, the spatial edges of the laser beam could not be detected, but we expect little variation of the temporal profile across the spatial domain.

III. GEOMETRIC OVERLAP OF TARGET AND BEAM

The key metric of the current study is the tin mass ($\tilde{m}$) geometrically overlapping the flat-top main-pulse laser beam (with diameter $\O_L$), which is calculated as

$$\tilde{m} = \rho \int_{\O_L} V \, dV. \tag{1}$$

Here, the tin volume enclosed within the sheet (V_{sheet}) is calculated as[14]

$$V_{\text{sheet}} = \int_{R_0}^{R(t)} 2\pi r h(r,t) \, dr, \tag{2}$$

where r denotes the radial coordinate along the sheet and t the expansion time. In our experiments, the expansion time is the time delay between the pre-pulse and the main-pulse laser beams. After some time $t \gg R_0/\dot{R}_0$ the sheet thickness profile may be approximated as[18]

$$h(r,t) \approx \frac{V_0}{\dot{R}_0 r t}, \tag{3}$$

where V_0 is the initial droplet volume and $\dot{R}_0$ is the initial expansion speed. More detailed representations of sheet profiles may be obtained from Liu et al.[14] (in turn inspired by droplet-pillar impact work by Wang et al.[19]). However, such profiles have a validity range that is too limited for the current study. Given that it is our central aim to understand the scaling relations underlying the mass use, rather than precise absolute numbers, we employ the simpler Eq. (3) in calculating the overlap volume (that is, the volume which geometrically overlaps with the beam spot) $\tilde{V}$ to arrive at

$$\tilde{V} = \frac{2\pi V_0}{\dot{R}_0} \int_{R_0}^{\O_L/2} \frac{1}{t} \, dr = \frac{2\pi V_0}{\dot{R}_0 t} [\O_L/2 - R_0]. \tag{4}$$

The integral limits are consistent with the initial droplet volume at $t = 0$ following the work of Villermaux et al.[18]. We note that $\O_T/2 > R_0$ in the following ($\tilde{V} = V_0$ otherwise). The resulting calculated overlap volume, normalized by the initial volume, is shown in Fig. 1(c) for different initial droplet diameters and pre-pulse laser energies. We control the initial droplet diameter (D_0) and, thus, droplet volume (V_0) by varying the modulation frequency applied to the nozzle. The initial expansion speed ($\dot{R}_0$) is varied by changing the pre-pulse laser beam intensity, which alters the pressure impulse on the droplet and, generically, results in different propulsion and expansion rates[15]. Accordingly, we can control the sheet thickness profile at the time of main-pulse laser impact by varying the droplet size, pre-pulse laser energy, and the pre-pulse to main-pulse delay time.

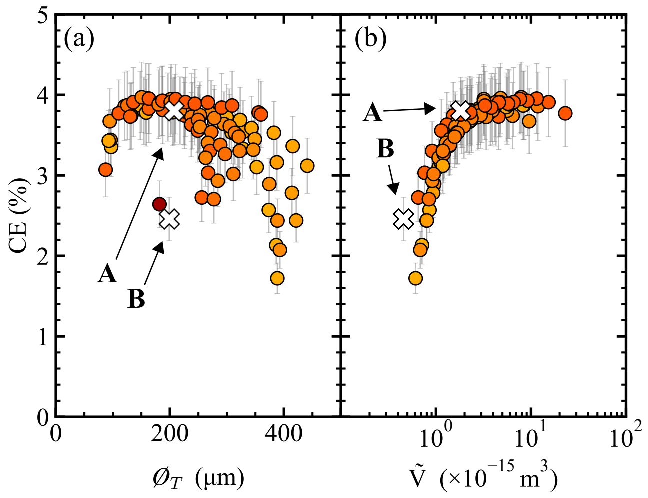

FIG. 2. Dependence of conversion efficiency (CE) on tin target parameters. Data points **A** and **B** indicate plasmas formed from similar target diameters but different thickness profiles obtained from the same droplet size and pre-pulse laser energy. (a) Experimentally measured CE as a function of tin target diameter using varying initial droplet diameter (D_0) and pre-pulse laser energy (E_{p}). Symbol color variation is used to indicate the diversity of data (simplified from Fig. 1 for better presentation). (b) Collapse of CE as a function of calculated overlap volume with the main-pulse laser (see the main text).

IV. RESULTS

Using different liquid tin droplet sizes and pre-pulse laser energies, we form tin sheets of different thickness profiles as measured and calculated in Fig. 1. After a predetermined time delay, the 2-µm-wavelength main-pulse laser impacts the tin target forming the EUV emitting plasma.

A. CE vs the volume overlapping the beam

The 2 µm-wavelength drive laser characteristics are kept constant at 11 ns time duration and an intensity of 7×10^{10} W/cm^2 which previously was shown to optimize CE. In Fig. 2(a), we show the conversion efficiency of laser light into EUV light as a function of the target diameter $\O_T$. The data shown are for targets generated using various pre-pulse energies and initial droplet sizes as shown in Fig. 1(b).

Tin targets that do not exhibit full geometrical overlap with the main-pulse laser result in a large fraction of the laser energy propagating past the target without any interaction. This effect trivially decreases the CE and targets with less than full geometrical overlap with the laser light are omitted from Fig. 2. Previous works, using very thick sheets, have demonstrated a very weak dependence of CE on target diameter for diameters larger than the main-pulse spot size [1,7]. Thus, the fact that a large fraction of the plasmas generated in the current study exhibit a lower-than-optimum CE, specifically those of large target diameters, is indicative of an additional

Journal of Applied Physics

AIP Publishing

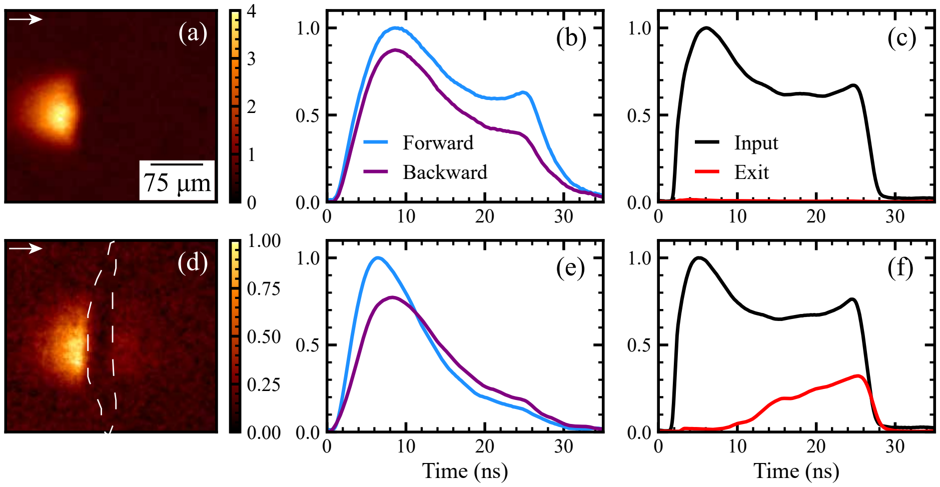

FIG. 3. Experimental observations of mass-limited laser produced plasma using a 23.8 ns long flat-top main-pulse. The top row shows a high-CE non-burnthrough case to be compared to the bottom row showing a mass-limited low-CE plasma. Panels (a) & (d) show time-integrated side-view images of the EUV emission for the high-CE and mass-limited cases, respectively. The color bars indicate the local emission intensity in arbitrary units. The laser impacts from the left as indicated by the white arrows. In panel (d), the dashed lines indicate a line-out of the curved tin sheet as observed using shadowgraphy imaging. The ratio of maximum (local) emission intensity between the two cases is 4:1. Panels (b) & (e) show the time-resolved normalized EUV emissions in the forward (21°) and backward (159°) with respect to the direction opposite to the laser light propagation. Panels (c) & (f) show the (normalized, see the main text) measured 2 µm laser light fired towards the tin sheet (input) and the transmitted light after the tin sheet or plasma at the exit of the vacuum chamber (exit).

limitation to CE: there is insufficient mass available to sustain plasma. To highlight this additional limitation to CE, we turn to two example targets **A** and **B**, which are preformed from the same droplet size using the same pre-pulse laser energy. The two targets have almost identical diameters (with full geometrical overlap with the main-pulse laser), but are observed at different expansion times. Target **A** is formed before and target **B** is formed after the apex time of the expansion trajectory, after the sheet contracts. At this latter time, it is well known that the continuous stretching and the loss of mass from the sheet itself[14] will have significantly reduced the target sheet thickness. Thus, we may expect that the main difference between the two targets is the thickness profile, as can be calculated from Eq. (4), see Fig. 1(c). The decreased CE in the target **B** case is subsequently attributed to the limited thickness and the insufficient overlap volume of the target.

In Fig. 2(b), we show the CE data shown in Fig. 2(a) as a function of the overlap volume as calculated by Eq. (4). We observe a collapse of the spread in CE shown in Fig. 2(a) onto a single curve, indicating off all parameters changes in our studies, only the available tin volume overlapping with the drive laser governs the obtainable CE. Targets **A** and **B** are highlighted to demonstrate that the difference in CE is explained from different overlap volumes. The CE-$\tilde{V}$ curve shown in Fig. 2(b) shows a plateau of efficiency beyond a certain overlap volume. For plasmas formed using smaller overlap volumes, the available tin mass is not sufficient to maintain the EUV-emitting plasma, and thus a lower CE is observed. For larger volumes, the CE plateaus near the optimum value for the 2 µm laser driver. Plasmas formed by tin sheets with very large overlap volumes have excess tin volume. The volume at which plasmas start to show near-peak CE (plateau) is around 2×10^{-15} m^3 for the current main-pulse settings.

The dependence of the CE of the generated plasmas on the overlap volume before the plateau region is observed in Fig. 2(b) to be sublinear with the dependence scaling approximately as $\mathrm{CE} \propto \tilde{V}^{0.6}$. This less-than-linear dependence cannot be straightforwardly explained, given the complex interplay between the mass flow from the liquid target towards the ablation front[20], and the resulting ever increasing acceleration of the remaining mass. As a side note, Fig. 2(b) indicates that the mass efficiency (i.e., the amount of photons per tin atom) monotonically increases with decreasing overlap volume (and CE).

B. Plasma limited by the available volume

Having established the overlap volume as the sole pertinent parameter limiting CE, we next aim to observe the effects of overlap volume on other plasma characteristics, such as the size and morphology of the emission area and the time-resolved dependencies. For mass-limited plasmas, we observe so-called "burnthrough" behavior, where the laser light ablates ("burns") through the available mass and eventually may propagate through the tin target and plasma. In Fig. 3(a), we show an EUV image (similar to Mostafa et al. [1]) of a high-CE plasma, sustained by a 107 µm diameter tin sheet of an average thickness of 2 µm overlapping the main-pulse. This target was preformed from a droplet with a particularly large initial diameter of 52 µm. For the same plasma, Fig. 3(b) shows normalized time-resolved measurements of the EUV light (as recorded on a fast EUV photodiode) emitted towards 21° (forward hemisphere) and towards 159° (backward hemisphere)

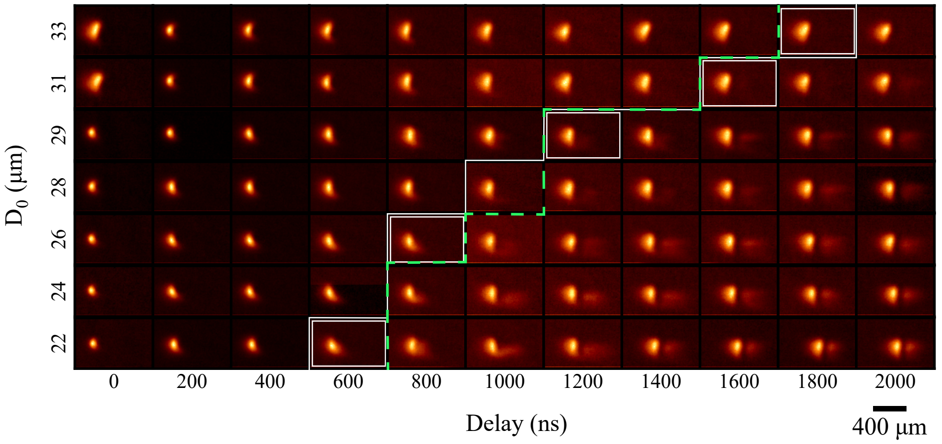

FIG. 4. Side-view images of the EUV emission from mass-limited plasmas generated by a 2 μm laser using different tin targets. All targets are preformed using a pre-pulse with energy 8 mJ. Various droplet sizes and delay times are used, as indicated along the respective axes. The sheet thickness decreases along the diagonal (from left-upper to right-lower corner. The white line separates mass-sufficient cases (left) from mass-limited cases (right). White boxes highlight cases of similar overlap volume (within ∼10 %) adjacent to the white line. The dashed green line presents the expectation from the power law $D_0 \sim t^{1/3}$ (see the main text). For the D_0=24 and 28 μm cases no equal volume (within ∼10 %) data is shown. A scale bar is shown at the bottom right.

with respect to the direction opposite to the laser light propagation. In Fig. 3(c), the measured laser light intensities at the entrance and exit of the vacuum chamber are shown to demonstrate the input and transmitted laser light, respectively.

In a high-CE plasma as shown in Fig. 3, the temporal EUV emission profile (b) closely follows that of the drive laser (c). In this mass-sufficient case, the EUV emission is sustained throughout the entire drive laser pulse, and no laser light at the exit of the chamber is observed [cf. Fig. 3(c)]. A low-CE plasma is generated using identical main-pulse parameters driving a 282 μm diameter tin sheet, preformed from a 20 μm diameter droplet. This larger sheet diameter and smaller initial droplet size, compared to the high-CE case, result in a target with very little mass. Fig. 3(d) shows the side-view image of the EUV emission from this plasma, which exhibits burnthrough characteristics: EUV light is emitted behind the target. The dashed line indicates the outline of the curved tin sheet as observed through side-view shadowgraphs. Behind the 'shadow' of the tin sheet, we observe EUV light emission which indicates a punch-through of the plasma and propulsion of the small amount of mass sustaining the plasma behind the sheet. There is also a clear observation of the reduction of emitted EUV (and consequently CE) at later times as shown in Fig. 3(e). The time at which the EUV emission deviates from following the laser profile [as is the case in Fig. 3(e)] highlights the time at which the available tin mass is no longer sufficient. This approximately matches with the time at which the laser light starts to transmit through the light source as shown in Fig. 3(f). We note that the EUV signals in forward and backward directions are individually scaled for visibility, with the backward-oriented photodiode observing a much smaller signal than its forward counterpart. A finite backward signal is also expected in cases of sufficient tin mass given the imperfect geometric blocking on the extended EUV emission volume by the remaining liquid. The laser photodiode traces in Fig. 3(c,f) are normalized to a common value, which is the maximum signal of the photodiode looking at the input laser light. We note that no correction for window transmission or beam propagation and its impact on scattering was made, although similar detection setups were used on input and exit side. Thus, the relative signal strengths are indicative only of the local laser fluence, and the focus should lie on the respective temporal evolution.

Next, in Fig. 4 we show EUV images for plasmas formed from seven different initial droplet diameters preformed into 10 different sheet diameters (and correspondingly, thicknesses). For this set of studies, we employ a spatially larger main-pulse of 144 μm in diameter. The impact of spatial beam size on CE (and EUV emission size) is reported in Ref. 1 The larger diameter of this laser setting allows us to take images significantly above the resolution limit of the EUV imaging setup (which is approximately 6.5 μm) and thus we can capture, in detail, the variation in the emission across the emission area. For decreasing droplet size and an increasing pre-pulse to main-pulse delay time, the average sheet thickness monotonically decreases [see Eq. (3)]. Subsequently, with decreasing sheet thickness, we observe burnthrough to occur, with ever more EUV light observed behind the sheet. The somewhat asymmetric EUV emission seen in such burnthrough cases can be directly correlated with the main-pulse laser's spatial intensity profile shown, see Ref. 1. Additional contributions to the asymmetry such as shadowing of the EUV light by tin vapor or liquid cannot be fully excluded and warrant further study. The white line drawn separates the mass-limited cases from non-burnthrough measurements, as determined visually from the images. Plasmas to the left of the white line show no demonstration of mass-limited behavior, while the images on the right show burnthrough of the EUV emission. White boxes shown in Fig. 4 indicate cases of similar overlap volume (within ∼10 %) adjacent to the white line.

We may again explain the scaling (of the white line and the boxes) from the overlap volume through the approximate scaling obtained via

$$\tilde{V} = \frac{2\pi V_0}{\dot{R}_0 t}\left[\varnothing_L/2 - R_0\right] \sim D_0^3/\dot{R}_0 t. \tag{5}$$

Given that $\dot{R}_0$ does not scale appreciably in the specific current setting and data selection [cf. Fig. 1(b)] for stable disk targets, we may consider it a constant and conclude that a constant $\tilde{V}$ is approximately obtained for $t \sim D_0^3$ or equivalently $D_0 \sim t^{1/3}$, in close agreement with the white line shown in Fig. 4. Generally $\dot{R}_0$ is a function of parameters such as D_0, $\varnothing_L$, and pulse energy[15], and its constancy is accidental. The factor of three variation in the burnthrough delay time, ranging from 600 to 1800 ns, is reasonably well captured by the scaling of the respective droplet radii $(33/22)^{1/3} \approx 3.4$. A dashed green line in Fig. 4 presents the expectation from the power law $D_0 \sim t^{1/3}$ with the prefactor set to match the $D_0 = 22\,\mu$m case. The observed close agreement again underlines the validity of using the overlap volume as a key predictor for mass limitations to high-CE operation of LPPs.

V. CONCLUSIONS

We investigated the mass use of 2 µm wavelength laser driven tin plasmas, and identified a key dependence of the conversion efficiency on the tin volume overlapping the laser beam. We observed that for plasmas driven under a CE-optimized laser intensity, 85 µm beam diameter and 11 ns pulse duration, an optimum overlap volume is approximately 2×10^{-15} m^3. Generating plasma using thicker tin sheets resulted in excess mass with no increase in CE. We note that increases in CE may still be possible using target shapes different from the current sheet targets, but this is as yet an unexplored topic for the specific case of 2 µm wavelength laser driven tin plasmas. Using thinner sheets resulted in laser burnthrough behavior where there is insufficient mass to maintain the tin plasma and consequently the CE decreases. We demonstrated key burnthrough metrics such as EUV emission imaging, time-resolved EUV emission anisotropy, and escaped laser light.

Industrial EUV sources employed for nanolithography generate plasma using a 10 µm wavelength laser driver of several-ten-nanoseconds[5,6]. Assuming such a system utilizes the entirety of the available tin mass, the energy-per-unit-volume can be calculated to be several 10^{15} mJ/m^3, as can be deduced from, e.g., Ref. 5. In our experiments, using a 2 µm wavelength laser driver of 11 ns pulse duration (producing 2.5 mJ in-band light), we calculate an energy efficiency of 7×10^{14} mJ/m^3 per laser shot, considering only the volume that overlaps the beam. This number is close, but the comparison to the state-of-the-art presents an active challenge at this stage. Of course, in our case there is much more mass introduced in our system than we account for only in the target-beam overlap: most of the mass as provided by the full droplet is not utilized for EUV generation as the target is pre-shaped to sizes much larger than beam diameter. With careful target shaping to minimize non-utilized mass[17], the initial tin volume can be driven closer to the overlapping volume which may enable mass use rates of the same order as in the state-of-the-art systems employed for nanolithography applications.

ACKNOWLEDGMENTS

This work was conducted at the Advanced Research Center for Nanolithography (ARCNL), a public-private partnership between the University of Amsterdam (UvA), Vrije Universiteit Amsterdam (VU), Rijksuniversiteit Groningen (UG), the Dutch Research Council (NWO), and the semiconductor equipment manufacturer ASML and was funded by the European Research Council (ERC StG 802648) and the Dutch Research Council (Vidi 15697 and OTP 19458). We would like to thank Iliya Cerjak and Henk-Jan Boluijt for their work designing the experimental setup and Laurens van Buuren for the aid in assembling the setup and its operation. We further thank Ruben Schupp and Muharrem Bayraktar for their help with the experimental work, as well as Lucas Poirier, Stan de Lange, and Michael Purvis for helpful discussions.

DATA AVAILABILITY STATEMENT

Data underlying the results presented in this paper may be obtained from the authors upon reasonable request.

DISCLOSURES

The authors declare no conflicts of interest.

[1] Y. Mostafa, L. Behnke, D. J. Engels, Z. Bouza, J. Sheil, W. Ubachs, and O. O. Versolato, Appl. Phys. Lett. **123**, 234101 (2023).
[2] C. W. Siders, A. C. Erlandson, T. C. Galvin, H. Frank, S. Langer, B. A. Reagan, H. Scott, E. F. Sistrunk, and T. M. Spinka, in *Proc. of EUV Source Workshop* (EUV Source Workshop, 2019).
[3] I. Tamer, B. A. Reagan, T. Galvin, J. Galbraith, E. Sistrunk, A. Church, G. Huete, H. Neurath, and T. Spinka, Opt. Lett. **46**, 5096 (2021).
[4] I. Tamer, B. A. Reagan, T. Galvin, F. Batysta, E. Sistrunk, D. Willard, A. Church, H. Neurath, J. Galbraith, G. Huete, and T. Spinka, Opt. Express **30**, 46336 (2022).
[5] K. Kouge, S. Nagai, T. Hori, Y. Ueno, T. Yanagida, K. Miyao, H. Hayashi, Y. Watanabe, T. Abe, H. Nakarai, T. Saito, and H. Mizoguchi, J. Photopolym. Sci. Technol. **33**, 37 (2020).
[6] M. A. van de Kerkhof, F. Liu, M. Meeuwissen, X. Zhang, M. Bayraktar, R. C. de Kruif, and N. V. Davydova, J. Micro/ Nanolithogr. MEMS MOEMS **19**, 033801 (2020).
[7] R. Schupp, L. Behnke, J. Sheil, Z. Bouza, M. Bayraktar, W. Ubachs, R. Hoekstra, and O. O. Versolato, Phys. Rev. Res. **3**, 013294 (2021).
[8] L. Behnke, R. Schupp, Z. Bouza, M. Bayraktar, Z. Mazzotta, R. Meijer, J. Sheil, S. Witte, W. Ubachs, R. Hoekstra, and O. O. Versolato, Opt. Express **29**, 4475 (2021).
[9] Y. Tao, M. S. Tillack, S. S. Harilal, K. L. Sequoia, R. A. Burdt, and F. Najmabadi, Opt. Lett. **32**, 1338 (2007).
[10] S. Fujioka, H. Nishimura, K. Nishihara, M. Murakami, Y.-G. Kang, Q. Gu, K. Nagai, T. Norimatsu, N. Miyanaga, Y. Izawa, *et al.*, Appl. Phys. Lett. **87** (2005).
[11] L. Rymell and H. Hertz, Rev. Sci. Instrum. **66**, 4916 (1995).

[12] R. Schupp, L. Behnke, Z. Bouza, Z. Mazzotta, Y. Mostafa, A. Lassise, L. Poirier, J. Sheil, M. Bayraktar, W. Ubachs, R. Hoekstra, and O. O. Versolato, J. Phys. D: Appl. Phys. **54**, 365103 (2021).

[13] R. A. Burdt, S. Yuspeh, K. L. Sequoia, Y. Tao, M. S. Tillack, and F. Najmabadi, J. Appl. Phys. **106**, 033310 (2009).

[14] B. Liu, D. Kurilovich, H. Gelderblom, and O. Versolato, Phys. Rev. Appl. **13**, 024035 (2020).

[15] J. Hernandez-Rueda, B. Liu, D. J. Hemminga, Y. Mostafa, R. A. Meijer, D. Kurilovich, M. Basko, H. Gelderblom, J. Sheil, and O. O. Versolato, Phys. Rev. Res. **4**, 013142 (2022).

[16] H. Gelderblom, H. Lhuissier, A. L. Klein, W. Bouwhuis, D. Lohse, E. Villermaux, and J. H. Snoeijer, J. Fluid Mech. **794**, 676–699 (2016).

[17] B. Liu, R. A. Meijer, W. Li, J. Hernandez-Rueda, H. Gelderblom, and O. O. Versolato, Phys. Rev. Appl. **20**, 14048 (2023).

[18] E. Villermaux and B. Bossa, J. Fluid Mech. **668**, 412–435 (2011).

[19] Y. Wang and L. Bourouiba, J. Fluid Mech. **969**, A19 (2023).

[20] M. M. Basko, V. G. Novikov, and A. S. Grushin, Phys. Plasmas **22**, 053111 (2015).